Inorganic Chemistry

Article

pubs.acs.org/IC

Structural and Spectroscopic Investigation of an Anilinosalen Cobalt Complex with Relevance to Hydrogen Production

Amélie Kochem,*[,†] Fabrice Thomas,[‡] Olivier Jarjayes,[‡] Gisèle Gellon,[‡] Christian Philouze,[‡] Thomas Weyhermüller,[†] Frank Neese,[†] and Maurice van Gastel*[,†]

[†]Max Planck Institute for Chemical Energy Conversion, Stiftstrasse 34-36, D-45470 Mülheim an der Ruhr, Germany

[‡]Département de Chimie Moléculaire-Chimie Inorganique redox Biomimétique (CIRE)−UMR CNRS 5250, Université J. Fourier, B. P. 53, 38041 Grenoble cedex 9, France

Supporting Information

ABSTRACT: A Co(II) anilinosalen catalyst containing proton relays in the first coordination sphere has been synthesized that catalyzes the electrochemical production of hydrogen from acid in dichloromethane and acetonitrile solutions. The complex has been spectroscopically and theoretically characterized in different protonation and redox states. We show that both coordinated anilido groups of the neutral Co(II) complex can be protonated into aniline form. Protonation induces an anodic shift of more than 1 V of the reduction wave, which concomitantly becomes irreversible. Hydrogen evolution that originates from the aniline protons located in the first coordination sphere is observed upon bulk electrolysis at −1.5 V of the protonated complex in absence of external acid. Structures for intermediates in the catalytic reaction have been identified based on this data.

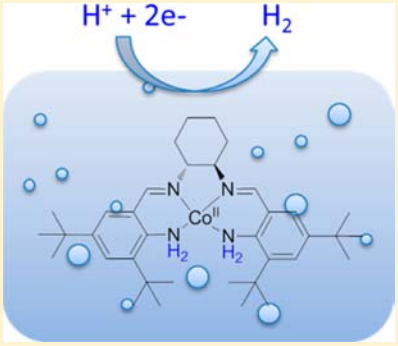

INTRODUCTION

Hydrogen (H_2) is a clean, renewable fuel, which has a very high energy density.[1−4] It is expected to become a major factor in the world's energy economy. Although platinum is an excellent catalyst for proton reduction and hydrogen oxidation, its high cost, low abundance, and long-term instability have stimulated the search for alternatives to produce hydrogen. Earth-abundant, inexpensive metals such as nickel and iron are found in hydrogenase enzymes, which regulate hydrogen metabolism in nature. [NiFe] and [FeFe] hydrogenases evolve hydrogen catalytically from water near the thermodynamic potential. Their efficiencies are comparable to platinium catalysts,[5,6] clearly showing that the use of noble metal is not strictly required for H_2 production. However, the large size and sensitivity of these enzymes to molecular oxygen have stimulated the search for well-defined molecular catalysts that can produce hydrogen from water in a nonbiological system. These considerations have resulted in the development of a variety of molecular catalysts that employ earth-abundant metals.[7−11] Synthetic complexes of nickel,[12−15] cobalt,[16−26] iron,[27−29] and molybdenum[30−32] have been developed recently as electrocatalysts for the production of hydrogen.

In the active site of the [FeFe] hydrogenase, the nitrogen of an azadithiolate ligand is proposed to mediate proton transfer at the distal iron atom, as shown in Scheme 1.[33] Several research groups have taken this motif and focused their efforts on the design and the study of H_2 production catalysts that involve first row transition-metal complexes and incorporate bases in the second coordination sphere. A prime example is a series of (bis-diphosphine)nickel complexes from the Dubois group.[34] In these catalysts, as well as in the [FeFe] hydrogenases, the presence and geometry of noncoordinating amine bases near the metal center have been shown to be a key requirement for efficient catalysis.[35] The pendant amines facilitate the cleavage or formation of the H−H bond and serve as proton relays during the catalytic cycle.[36] Since up to four pendant amine bases are incorporated in the second

Scheme 1. (a) Proposed Structure of the [FeFe] Hydrogenase Active Site Based on Crystallographic Data[6] and (b) Structures of the Initial Cobalt(II) Complexes Investigated in This Study and of the Salen Counterpart Complex 2

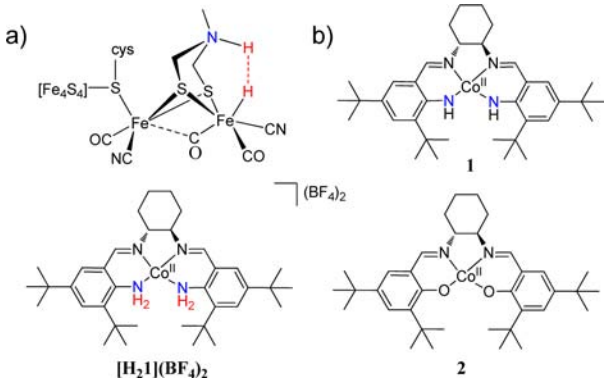

Received: November 11, 2013
Published: November 22, 2013

coordination sphere in the Dubois catalysts, multiple isomers could in principle be obtained in solution, and it has been shown that not all of them are in a catalytically active form.[37] The catalytic rates are found to be highly sensitive to the presence and arrangement of pendant amines in the ligand.

In the field of the biomimetic chemistry of the active of [NiFe] hydrogenases, nickel-based complexes with protonable ligands such as thiolato or amidato ligands in the first coordination sphere have been reported.[38−43] One of these complexes, which features phosphine ligands, has an activity of 50−75 s^{-1} at an overpotential of 430 mV.[38,39] Surprisingly, only few studies have been carried out on cobalt catalysts incorporating proton relays in the first coordination sphere.[44] Photochemical hydrogen evolution reaction (HER) using a $[Fe^{II}(opta)_3](ClO_4)_2$ complex has been described,[45] as well as coordinatively saturated octahedral hexa-amino cobalt complexes[46] which catalyze the electroproduction of hydrogen. In both cases, at least two amino groups are directly bound to the metal center. These groups have been proposed as the bases for H^+ in the photochemically or electrochemically evolved H_2. To the best of our knowledge, cobalt-based compounds including bases in the first coordination sphere and vacant or labile coordination site suitable for hydrido binding have not been described so far.

Here we report a new cobalt complex based on a stable tetradentate anilinosalen ligand that is active toward hydrogen production. This ligand, provides a tetra-aza coordination sphere (Scheme 1, complex **1**).[47] The choice of this ligand was motivated by several attractive features. First, in analogy to parent salen complexes, the oxidation and reduction potentials can be easily modulated by the anilido substituents.[48] Second, the structural distortions which are known to influence the reduction potentials at the metal centers can be easily controlled by the nature of the bridge.[49] Third, this type of ligand is known to stabilize the cobalt center in the Co^{I}, Co^{II}, and Co^{III} redox states.[50,51] These states are involved in most of the reported catalytic mechanisms for hydrogen production from cobalt complexes.[52] Lastly, replacement of the phenolate groups in the classical salen ligand by anilido groups gives rise to the presence of bases in the first coordination sphere. We show here that although the electron donating *tert*-butyl substituents of the anilido groups make the complex robust toward reduction, these bases can be protonated into anilines. This leads to a positively charged complex with a softer coordination sphere around the metal center, which can be much more easily reduced (Scheme 1, complex $[\mathbf{H_21}](\mathbf{BF_4})_2$). In contrast to anilido complexes, aniline complexes cannot be easily oxidized to anilino radical, meaning that the redox chemistry is metal centered.[53] By a combination of electrochemistry and spectroscopy, we establish that the produced H_2 derives from these anilino groups. The rigid arrangement of the bases and thereby the positions of the protons near to the reactive metal center can be easily controlled by the ligand framework. We show that the proton relays in the first coordination sphere of the metal center have a crucial role in the catalytic pathway and identify intermediates in the catalytic cycle. Additionally, to facilitate the interpretation of the cyclic voltammetry (vide infra) we synthesize and characterize the nonprotonated monooxidized species in presence of exogenous donors (*N*-methylimidazole). Under such conditions, the oxidation process is found to be metal centered, giving rise to the genuine octahedral Co(III)-bis(anilido) complex [**1-im**]-$\mathbf{ClO_4}$.

RESULTS AND DISCUSSION

Synthesis of the Ligand and Metalation. The anilinosalen ligand and the corresponding cobalt complex **1** have been obtained in high yields. The ligand was synthesized following a recently published method.[47] The low spin cobalt(II) complex **1** was obtained by metalation of the anilinosalen ligand with $Co(OAc)_2{\cdot}4H_2O$ under anaerobic conditions in methanol. Treatment of a dichloromethane solution of **1** under inert atmosphere with 2 equiv of $HBF_4{\cdot}Et_2O$ at room temperature resulted in immediate color change from red to yellow. The so-formed protonated compound has been isolated in quantitative yield as tetrafluoroborate salt $[\mathbf{H_21}](\mathbf{BF_4})_2$ forming a yellow microcrystalline solid. This complex allows reversible deprotonation by addition of Et_3N, restoring **1**. Aerobic oxidation of a methanolic:CH_2Cl_2 solution of **1** in the presence of three molar equivalents of *N*-methylimidazole followed by addition of $NaClO_4$ yields the diamagnetic complex $[\mathbf{1\text{-}im}]\mathbf{ClO_4}$.

Geometric and Electronic Structure of the Co(II) Complexes 1 and $[H_21](BF_4)_2$. *Structural Characterization.* The unit cell of **1** (Table 1) contains four crystallographically independent molecules with similar bond lengths and angles. The solid state structure of one representative molecule is shown in Figure 1a, bond lengths are summarized in Table 2. **1** displays a cobalt(II) ion coordinated by four nitrogen atoms, two symmetry-equivalent imino nitrogen atoms, N1 and N2, and two symmetry-equivalent anilido nitrogen atoms, N3 and N4. The dihedral angle between N1−Co−N4 and N2−Co−N3 planes is 12.5°. The N3−Co−N4, N4−Co−N1, N1−Co−N2, and N2−Co−N3 angles differ only slightly from 90° (91.1(2),

Table 1. Crystallographic Data for 1, $[H_21](BF_4)_2$ and $[1\text{-}im_2]ClO_4$

	1	$[\mathbf{H_21}](\mathbf{BF_4})_2$	$[\mathbf{1\text{-}im_2}]\mathbf{ClO_4}$
chem. formula	$C_{41}H_{59}CoN_5$	$C_{37}H_{58}B_2Cl_2CoF_8N_4$	$C_{45}H_{70}ClCoN_8O_5$
Fw	680.86	862.32	897.47
space group	$P2_1$, No. 4	$C2$, No. 5	$P2_12_12_1$, No. 19
a, Å	16.649(3)	20.508(3)	9.866(3)
b, Å	17.767(4)	17.289(2)	15.732(3)
c, Å	26.115(5)	12.615(2)	31.273(7)
β, deg	92.05(2)	114.389(2)	90
V, Å	7720(3)	4073.7(10)	4854(2)
Z	8	4	4
T, K	200(2)	100(2)	200(2)
ρ calcd, g cm^{-3}	1.172	1.406	1.228
refl. collected/ $2\Theta_{max}$	69949/55.02	60277/62.22	18731/50.00
unique refl./ $I > 2\sigma(I)$	33742/24021	13105/11924	4622/4025
no. of params/ restr.	1801/196	501/1	557/4
λ, Å/*μ*(K*α*), cm^{-1}	0.71073/4.78	0.71073/6.22	0.71073/4.59
R1[a]/goodness of fit[b]	0.0466/1.065	0.0308/1.045	0.0533/1.098
wR2[c] ($I > 2\sigma(I)$)	0.1018	0.0801	0.1322
absol. structure param	−0.030(9)	0.029(4)	0(10)
residual density, e $Å^{-3}$	+0.30/−0.40	+0.67/−0.80	+0.61/−0.37

[a]Observation criterion: $I > 2\sigma(I)$. R1 = $\sum||F_o| - |F_c||/\sum|F_o|$. [b]GoF = $[\sum[w(F_o^2 - F_c^2)^2]/(n - p)]^{1/2}$. [c]wR2 = $\{\sum[w(F_o^2 - F_c^2)^2]/\sum[w(F_o^2)^2]\}^{1/2}$ where $w = 1/\sigma^2(F_o^2) + (aP)^2 + bP$, $P = (F_o^2 + 2F_c^2)/3$.

dx.doi.org/10.1021/ic402818g | *Inorg. Chem.* 2013, 52, 14428−14438

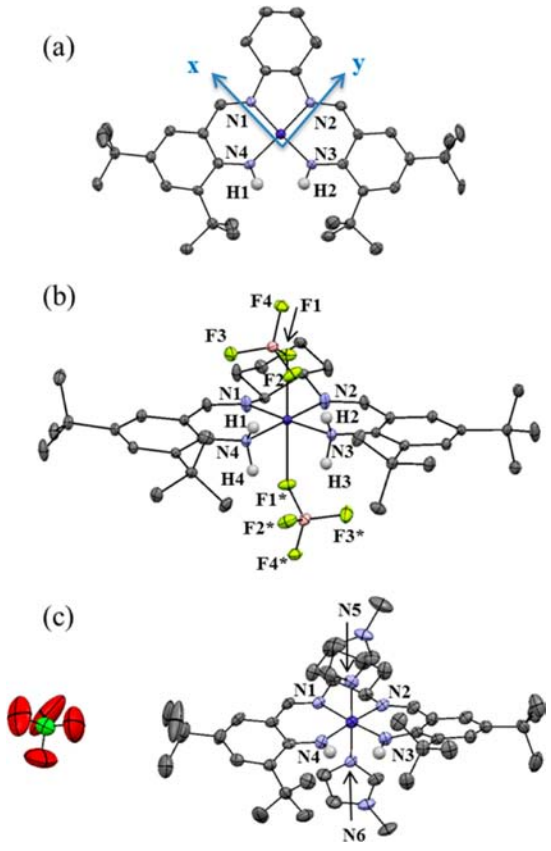

Figure 1. X-ray structures of (a) **1**, (b) $[\mathbf{H_21}](\mathbf{BF_4})_2$, and (c) $[\mathbf{1\text{-}im}]\mathbf{ClO_4}$ shown with 50% thermal ellipsoids and with the coordinate system used in the discussion. H atoms are omitted except for the ones of the anilido/anilino groups.

Table 2. Comparison of Experimental and Calculated Bond Lengths of the First Coordination Sphere (Å) for 1 and $[\mathbf{H_21}](\mathbf{BF_4})_2$

bond	**1** (exp)	**1** (calc)	$[\mathbf{H_21}](\mathbf{BF_4})_2$ (exp)	$[\mathbf{H_21}](\mathbf{BF_4})_2$ (calc)
Co−N4	1.844(3)	1.852	1.984(2)	1.999
Co−N3	1.842(3)	1.853	1.984(2)	2.019
Co−N1	1.855(3)	1.860	1.890(2)	1.883
Co−N2	1.861(3)	1.861	1.890(2)	1.881

91.8(1), 86.4(1) and 92.0(1)° respectively). The geometry around the metal ion is thus essentially square planar with the hydrogen atoms of the anilido groups pointing in the equatorial plane of the molecule. The Co−N1, Co−N2, Co−N3, and Co−N4 bond lengths are 1.855(3), 1.861(3), 1.842(3), and 1.844(3) Å, respectively. Note that these Co−N bond lengths are roughly comparable with those in other cobalt anilinosalen complexes.[54] This is consistent with a low-spin configuration for the cobalt(II) ion, which has been further confirmed by electron paramagnetic resonance (EPR) spectroscopy (vide infra).

Diffusion of pentane into a concentrated solution of $[\mathbf{H_21}]^{2+}$ in dichloromethane results in formation of single crystals of $[\mathbf{H_21}](\mathbf{BF_4})_2$ suitable for X-ray crystallography. The unit cell of $[\mathbf{H_21}](\mathbf{BF_4})_2$ contains two independent molecules with similar metric parameters. Each of them resides on 2-fold axes, and the pairs N3/N4 and N1/N2 are symmetry equivalent crystallographically. The structure of one representative molecule is depicted in Figure 1b, and the bond lengths are summarized in Table 2. The cobalt ion in $[\mathbf{H_21}]^{2+}$ resides in an octahedral ligand field with two BF_4^- counterions coordinated in the axial positions. The two BF_4^- molecules are weakly coordinated at the same Co−F bond distance of 2.301(1) Å. The Co−N1, Co−N2, Co−N3, and Co−N4 bond lengths are at 1.890(2), 1.890(2), 1.984(2), and 1.984(2) Å, respectively. The dihedral angle between N1−Co−N4 and N2−Co−N3 planes is 6.7°. N3−Co−N4, N4−Co−N1, N1−Co−N2, and N2−Co−N3 angles are at 88.65(13), 93.09(9), 85.58(14), and 93.09(9)° respectively. Weak hydrogen bonds are formed between hydrogen atoms of the anilino groups and fluoride atoms of the BF_4^- (see Supporting Information, Table S3). In the solid state the structure is highly symmetric with the two counterions equally weakly bound to both sides of the molecule. The conformation of the NH_2 groups involving H1, H2, H3, and H4 displays a small amount of staggering of 9°. While the Co−N1 and Co−N2 bond lengths are elongated by only 0.03 Å in $[\mathbf{H_21}]^{2+}$, the Co−N3 and Co−N4 bond lengths are significantly longer (+0.14 Å) than those in the starting neutral complex **1**. Protonation of the anilido groups to anilines thus leads to a much softer coordination sphere, since the anilido group is an anionic σ and π donor whereas the aniline is a neutral σ donor.

Density functional theory (DFT) calculations were performed at the BP86 level of theory for **1** and $[\mathbf{H_21}](\mathbf{BF_4})_2$ by considering an (S = 1/2) ground spin state (Supporting Information, Figures S1 and S2). The bond distances calculated by geometry optimization match those of the X-ray structures to within 0.01 Å and 0.035 Å (Table 2) in the case of **1** and $[\mathbf{H_21}](\mathbf{BF_4})_2$, respectively. As was the case in the crystal structures, the calculated Co−N bond distances are elongated when going from **1** to $[\mathbf{H_21}](\mathbf{BF_4})_2$, while a larger angle between the N1−Co−N4 and N2−Co−N3 planes is found in **1** (13.96°) in comparison with $[\mathbf{H_21}](\mathbf{BF_4})_2$ (1.06°).

cw-EPR Spectroscopy. All spectroscopic and electrochemical experiments have been performed on samples that have been purified by crystallization. The 10 K continuous-wave (cw) X-Band EPR spectra of **1** and $[\mathbf{H_21}](\mathbf{BF_4})_2$ in CH_2Cl_2 are depicted in Figure 2. The spectrum of **1** displays a nearly axial (S = 1/2) signal with hyperfine splitting into eight lines in the high field component. The spectrum of $[\mathbf{H_21}](\mathbf{BF_4})_2$ displays a more rhombic (S = 1/2) signal with hyperfine splitting in the high and low field components. In both cases, the hyperfine splitting arises from the interaction of the electron spin with the cobalt nucleus (I_{Co} = 7/2). The simulation parameters (see Figure 2) point to a dominant d_{yz} or d_{xz} electronic ground state for **1** and to a main d_{z^2} electronic ground state for $[\mathbf{H_21}](\mathbf{BF_4})_2$. The EPR data are thus consistent with a square planar geometry for a d^7 metal ion for **1** and with an octahedral geometry for $[\mathbf{H_21}](\mathbf{BF_4})_2$, and indicate that the cobalt(II) complexes largely retain their solid state structure in CH_2Cl_2 solution.

DFT calculations on the geometry-optimized complexes **1** and $[\mathbf{H_21}](\mathbf{BF_4})_2$ confirm the localized, metal-based character of the singly occupied molecular orbital (SOMO) for both **1** (30% d_{z^2}, 28% d_{xz}, 30% d_{yz}) and $[\mathbf{H_21}](\mathbf{BF_4})_2$ (90% d_{z^2}). Plots of the SOMOs are given in the Supporting Information, Figures S4 and S5.

Interactions with Surrounding Protons, ^{1}H Davies ENDOR Spectroscopy. ^{1}H electron nuclear double resonance (ENDOR) spectroscopy is ideally suited to locally probe the electronic structure of the complex. By measuring the magnetic

dx.doi.org/10.1021/ic402818g | Inorg. Chem. 2013, 52, 14428−14438

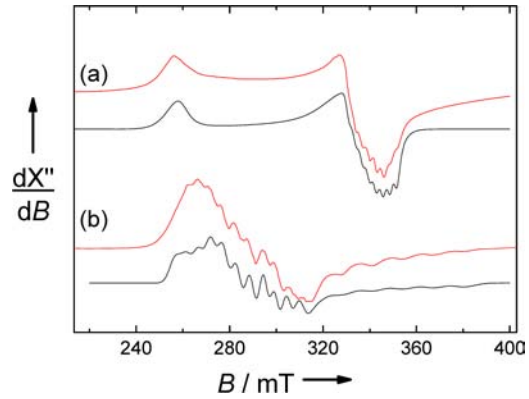

Figure 2. X-band EPR spectra of (a) **1** and (b) $[\mathbf{H_21}](\mathbf{BF_4})_2$ in 10 mM CH_2Cl_2 solution. Red lines: Experimental spectrum, black lines: simulation using Easyspin; parameters g_z = 2.635 g_y = 2.005, g_x= 1.985 (g_{iso} = 2.21), $A_{x(Co)}$ = 82 MHz, *g*-strain = [0.12, 0.12, 0.013], and hyperfine Strain = [80, 30, 0] MHz for **1** and g_x= 2.450, g_y = 2.295, g_z = 2.013, $A_{x(Co)}$ = 185 MHz, $A_{y(Co)}$ = 155 MHz, $A_{z(Co)}$ = 360 MHz, *g*-strain = [0.02, 0.02, 0.06], and hyperfine strain = [20, 55, 0] MHz for $[\mathbf{H_21}](\mathbf{BF_4})_2$. Microwave Freq.: 9.47 GHz; Power: 20 mW; Mod. Amp.: 0.5 mT, *T* = 10 K.

interaction between the electron spin and the surrounding ^{1}H nuclear spins that serve as local probes, the effective distance between the unpaired electron and the proton can be extracted. ENDOR spectroscopy is even more useful in our case because the protonation state of the molecule changes during the catalytic cycle. We have thus recorded orientation-selected ^{1}H Davies ENDOR spectra for the neutral species **1** at 34 GHz (Q-band). The Q-band EPR spectra along with the magnetic field settings where the ENDOR spectra have been recorded are shown in Figure 3, and the ENDOR spectra are shown in Figure 4, where the magnetic field value is indicated to the right of each spectrum. The ENDOR spectra of **1** display drastic changes with varying magnetic field settings, and all prominent signals are symmetrically distributed around ν_H. At the highest magnetic field setting (at $g_\perp$, position 1, see Figure 4 and Figure

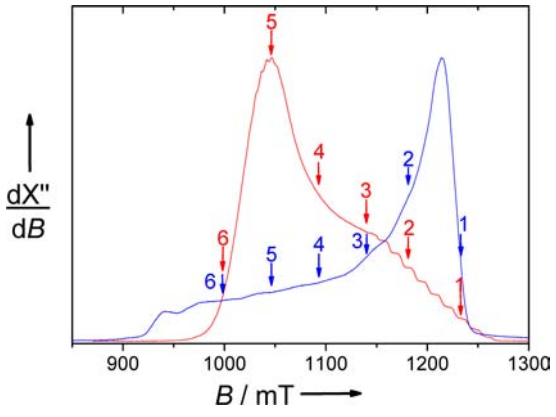

Figure 3. Q-band two-pulse echo-detected EPR spectrum of a 10 mM solution of **1** in CH_2Cl_2 (blue line) and Q-band pulse FID detected EPR spectrum of a 10 mM solution of $[\mathbf{H_21}](\mathbf{BF_4})_2$ in CH_2Cl_2 (red line). Numbers 1 to 6 indicate the field positions for which ^{1}H ENDOR spectra are shown (see Figure 4). Experimental parameters: **1**: frequency, 33.982 GHz; length of 90° pulse 40 ns; time between pulses, 150 ns; repetition rate, 8 kHz; temperature, 10 K; $[\mathbf{H_21}](\mathbf{BF_4})_2$: frequency, 34.035 GHz; length of 90° pulse 600 ns; repetition rate, 8 kHz; temperature, 10 K.

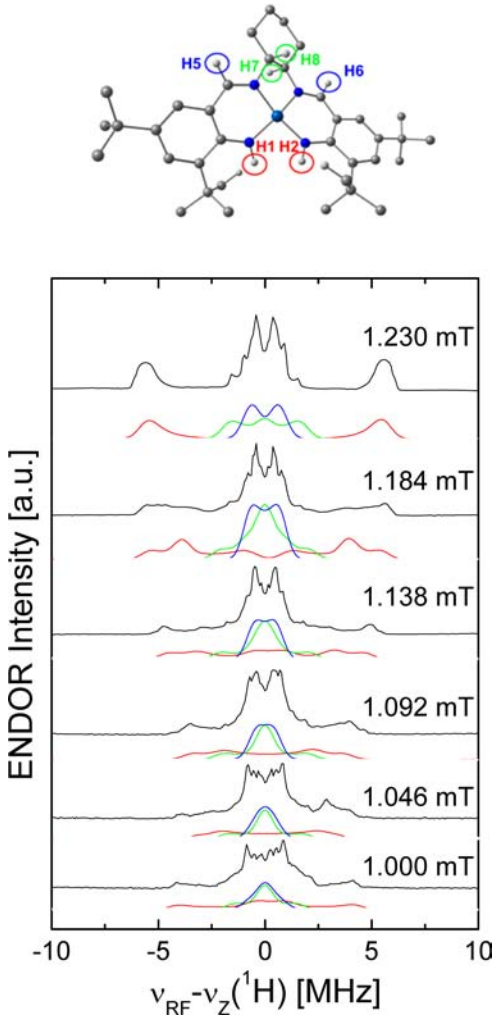

Figure 4. (top) Geometry-optimized structure of **1** showing the hydrogen atoms with the strongest hyperfine coupling constants. (bottom) Q-band Davies ENDOR spectra of **1** 10 mM in CH_2Cl_2. Experimental conditions: ν_{mw} = 33.875 GHz, *T* = 10 K, π_{RF} = 14 μs, length of 180 degree pulse 296 ns.

3) only one strong signal with a hyperfine coupling of 11 MHz is observed together with multiple narrower bands with hyperfine couplings smaller than 3 MHz. The latter bands are also present in all measurements at lower magnetic fields. The large coupling is expected to arise from protons near to the cobalt atom, which carries the bulk spin density. The most nearby protons are those of the NH groups of the two anilido moieties. Given the observation that both sides of the ligand are symmetric and that the complex is nearly planar, all symmetry related protons will be magnetically equivalent. Measurements at lower magnetic fields (position 2 and 3, Figure 4 and Figure 3) lead to a decrease of the effective hyperfine coupling constant of the anilido protons, concomitant with a lower intensity of this signal. The signal becomes small when approaching $B_0 \parallel g_z$ (position 6, Figure 4 and Figure 3) and multiple broad transitions with hyperfine coupling constants ranging between 3 and 9 MHz appear.

To simulate the ^{1}H ENDOR spectra, the calculated couplings from the DFT calculations have been used as starting parameters. It turned out that the initial simulations already reproduce all bands in the ENDOR spectra, indicating that the symmetric structure found in the DFT calculations represents a

dx.doi.org/10.1021/ic402818g | *Inorg. Chem.* 2013, 52, 14428−14438

good model for **1**. Minor optimization of the parameter set was necessary to obtain quantitative agreement between experiment and theory. The starting and the optimized parameter sets are given in the Supporting Information, Table S1, and the simulations are included in Figure 4. The bands with the largest shifts all belong to the anilido protons H1 and H2 and in particular the observation of only one band at the single-crystal-like g_x canonical orientation (position 1) provides direct information of the equivalence of both anilido groups.

Additionally, Q-band (34 GHz) orientation-selected ^{1}H Davies ENDOR spectra have been recorded for the diprotonated species $[\mathbf{H_21}](\mathbf{BF_4})_2$ to obtain detailed information about the delocalization of spin density especially near the hydrogen atoms of the anilido groups. They are shown in Supporting Information, Figure S7. A few signals are not symmetric around ν_H at high magnetic fields (position 6, 5, 4 and 3, Figure 3 and Supporting Information, Figure S7) and belong to the ^{19}F atoms of the counterions. Additionally, ^{11}B signals have been observed in the ENDOR spectra near the ^{11}B Zeeman frequency of 4.78 MHz (Supporting Information, Figure S6). These signals belong to the two BF_4^- counterions coordinated in the axial positions.

The signals that are symmetric around the ^{1}H Zeeman frequency exhibit smaller variation with changing magnetic field settings as compared those of **1**. Except for one low-intense shoulder at 1.056 mT no signals with hyperfine couplings larger than 7 MHz are present in the spectra. This is consistent with the changed SOMO, which for $[\mathbf{H_21}](\mathbf{BF_4})_2$ features a d_{z^2} contribution at Co with essentially no spin density at the anilino groups, thus giving rise to a decreased magnetic dipole interaction between the unpaired electron and the anilino protons as compared to **1**.

The simulations of the ENDOR spectra with parameters obtained from DFT calculations qualitatively reproduce both the number of bands observed in the ENDOR spectra and the hyperfine shifts to within 1.5 MHz (Supporting Information, Figure S7, Table S2). Moreover, the simulations reproduce the low-intense signal with a hyperfine coupling constant of 12 MHz at low magnetic field only when the structure involving two anilino groups in a staggered conformation is considered. Optimization of the parameter set for $[\mathbf{H_21}](\mathbf{BF_4})_2$ was unfortunately not feasible because almost all effective hyperfine coupling constants appear to be below 7 MHz, giving rise to strongly overlapping contributions of each proton. Nevertheless, based on the qualitative agreement of experiment and simulation based on DFT parameters of the staggered structure, in particular, with respect to the low-intense shoulder at 12 MHz, the ENDOR spectra support the asymmetric, staggered structure.

This observation gives important information about the mechanism of catalytic proton reduction. First, the complex is apparently flexible enough to adapt a staggered conformation in solution; at room temperature it may even undergo dynamic changes in which either of the two sets of protons of the anilino groups undergoes the distortion. Second, the staggering gives rise to nonequivalent protons, which consequently have different acidities. DFT calculations indeed confirm that the proton, which has moved maximally out of the equatorial plane is the most acidic one. It is the most likely candidate to become a hydride in a putative Co(III)-hydride transition state after further reduction of $[\mathbf{H_21}](\mathbf{BF_4})_2$.

Electronic Absorption Spectroscopy. The visible spectrum of **1** is shown in Figure 5. It is characterized by several intense

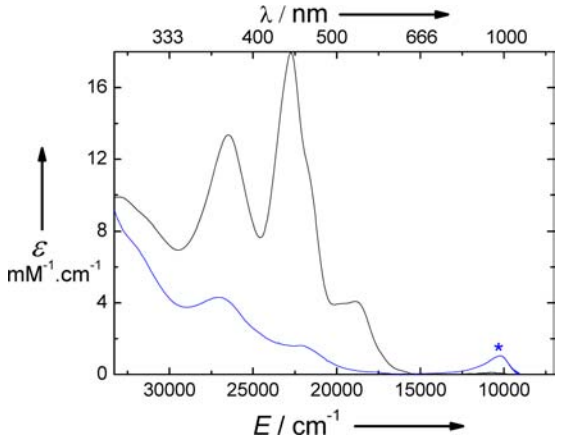

Figure 5. UV−visible spectra of solutions of the neutral and protonated complexes in 0.05 mM CH_2Cl_2 solutions: **1** (black) and $[\mathbf{H_21}](\mathbf{BF_4})_2$ (blue). T = 298K, inert atmosphere. The asterisk indicates a transition attributed to the monooxidized complex $\mathbf{1}^+$ impurity.

transitions at 26596 cm^{-1} (13.4 × 10^3 M^{-1} cm^{-1}), 22676 cm^{-1} (17.9 × 10^3 M^{-1} cm^{-1}) with a shoulder at 21598 cm^{-1} (12.6 × 10^3 M^{-1} cm^{-1}) and 18832 cm^{-1} (4.0 × 10^3 M^{-1} cm^{-1}) (Figure 5). On the basis of their high intensity, these transitions are assigned to charge transfer (CT) transitions. Protonation of the anilido groups in $[\mathbf{H_21}](\mathbf{BF_4})_2$ as compared to **1** leads to the disappearance of the transition at 18832 cm^{-1} (4042 M^{-1} cm^{-1}), while the intensity of the higher energy bands decreases strongly. The visible spectrum of $[\mathbf{H_21}](\mathbf{BF_4})_2$ does not change in the presence of a large excess of acid indicating that the protonation at the metal does not take place directly (see Supporting Information). Protonation is reversible, as confirmed by the recovery of the original UV−vis spectrum upon addition of triethylamine. The exact nature of the orbitals involved in the CT transitions was investigated by time-dependent DFT (TD-DFT) calculations. For **1** the principal electronic excitations that contribute to the CT bands at 26596 cm^{-1}, 22676 cm^{-1}, 21598 cm^{-1}, and 18832 cm^{-1} are calculated at ν_{calc} = 24160 cm^{-1} (f = 0.009), ν_{calc} = 22090 cm^{-1} (f = 0.023), ν_{calc} = 21626 cm^{-1} (f = 0.007), and ν_{calc} = 18914 cm^{-1} (f = 0.003), respectively, see Table 3. Difference transition

Table 3. Calculated Electronic Excitations[a]

complex	ν, cm^{-1}	(f)
1	24160	(0.009)
	22090	(0.023)
	21626	(0.007)
	18914	(0.003)
$[\mathbf{H_21}](\mathbf{BF_4})_2$	27382	(0.011)
	23213	(0.012)

[a]In CH_2Cl_2.

density plots for each transition are shown in Figure 6. The calculated transitions at 24160 cm^{-1}, 22090 cm^{-1}, and 21626 cm^{-1} correspond to metal-to-ligand charge-transfer (MLCT) transitions. In all three cases, the donor molecular fragment exhibits mostly a metal character with a d_{z^2} contribution for the transition at 24160 cm^{-1}, and d_{xz}, d_{yz} contributions for the transitions at 22090 cm^{-1} and 21626 cm^{-1}, respectively, while the acceptor one is a delocalized π orbital dominantly involving the two imino moieties. For the transition calculated at 18914

dx.doi.org/10.1021/ic402818g | Inorg. Chem. 2013, 52, 14428−14438

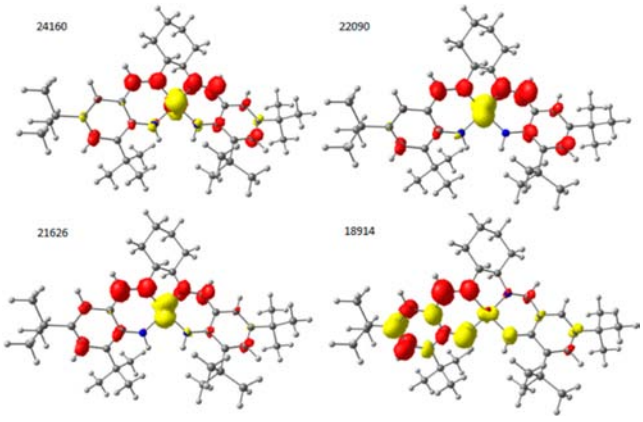

Figure 6. TD-DFT assignment of the electronic transitions of **1**. The diagrams give difference electron densities where red corresponds to positive density and yellow to negative density.

cm^{-1}, the donor molecular fragment corresponds to a delocalized π orbital involving the two anilido groups, while the acceptor one is a delocalized π orbital involving mostly one imino moiety and one anilido group. Thus, this transition corresponds to a LLCT, or alternatively a $\pi \rightarrow \pi^*$ transition. The computed transition energies are in excellent agreement with the experimental ones except for the electronic transition at highest energy, which is slightly overestimated (ν_{exp} = 26596 cm^{-1}, ν_{calc} = 24160 cm^{-1}).

In $[\mathbf{H_21}](\mathbf{BF_4})_2$ the principal electronic excitations that contribute to the CT band at 27100 cm^{-1} (4.3 × 10^3 M^{-1} cm^{-1}) and 22173 cm^{-1} (1.6 × 10^3 M^{-1} cm^{-1}) are calculated at ν_{calc} = 27382 cm^{-1} (f = 0.011) and ν_{calc} = 23213 cm^{-1} (f = 0.012) (Table 3). According to the difference transition densities (Figure 7), the donor molecular fragment for the

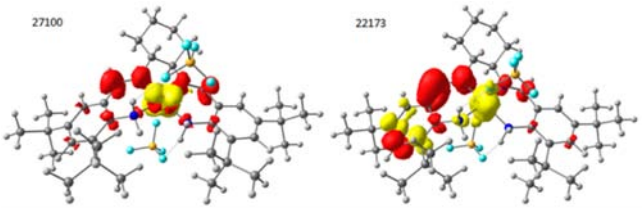

Figure 7. TD-DFT assignment of the electronic transitions in $[\mathbf{H_21}](\mathbf{BF_4})_2$. The diagrams give difference electron densities where red corresponds to positive density and yellow to negative density.

transition calculated at 23213 cm^{-1} exhibits mostly a metal character with d_{xz}, d_{yz} contributions, while the acceptor one is a delocalized π orbital involving mostly the two imino moieties. In the transition calculated at 27382 cm^{-1}, the donor molecular fragment exhibits mostly a metal character with d_{yz} contribution with a contribution of a π orbital of one anilino group, while the acceptor orbital is a delocalized π orbital involving mostly the two imino moieties and the two anilino groups. Both are MLCT transitions. Experimentally (Table 4), the intensity of the transition at 22173 cm^{-1} (1.6 × 10^3 M^{-1} cm^{-1}) is lower than for the one at 27100 cm^{-1} (4.3 × 10^3 M^{-1} cm^{-1}). Despite the fact that the oscillator strength of the transition calculated at 23213 cm^{-1} (f = 0.012) is found to be a little higher than for the one calculated at 27382 cm^{-1} (f = 0.011), calculations predict correctly the disappearance of the CT band at 18832 cm^{-1} and the lower intensity of the MLCT at higher energy on

Table 4. Experimentally Observed Transition Energies and Absorption Coefficients[a]

complex	ν_{max}, cm^{-1} (ε, 10^3 M^{-1} cm^{-1})
1	26596 (13.4), 22676 (17.9), 21598 sh (12.6), 18832 (4.0)
$[\mathbf{H_21}](\mathbf{BF_4})_2$	27100 (4.3), 22173 (1.6), 10183 br (1.0)

[a] In CH_2Cl_2 solution, T = 298 K. Abbreviations used: sh, shoulder ; br, broad.

going from **1** to $[\mathbf{H_21}](\mathbf{BF_4})_2$. Thus, based on the good agreement between experiment and theory, the TD-DFT calculations further support the presence of $[\mathbf{H_21}](\mathbf{BF_4})_2$ with coordinated counterions in solution at room temperature.

Geometric and Electronic Structure of the One Electron Oxidized Complex in the Presence of *N*-methylimidazole. *Structural Characterization.* In the presence of *N*-methylimidazole the oxidation of the neutral species **1** to the corresponding monocation was realized simply by aerobic incubation, due to the low $E_{1/2}$[2] value under these conditions (see electrochemistry part). Addition of $NaClO_4$ to the resulting solution initiates the crystallization of the diamagnetic $[\mathbf{1\text{-}im}]\mathbf{ClO_4}$ complex. Its structure is depicted in Figure 1, and coordination bond lengths are summarized in Table 5. The cobalt ion in $[\mathbf{1\text{-}im}]^+$ resides in an octahedral

Table 5. Comparison of Experimental and Calculated Coordination Sphere Bond Lengths (Å) for $[\mathbf{1\text{-}im}]\mathbf{ClO_4}$

bond	$[\mathbf{1\text{-}im}]\mathbf{ClO_4}$ (exp)	$[\mathbf{1\text{-}im}]\mathbf{ClO_4}$ (calc)
Co−N4	1.892(4)	1.928
Co−N3	1.898(4)	1.931
Co−N1	1.907(4)	1.922
Co−N2	1.907(4)	1.925
Co−N5	1.987(5)	1.976
Co−N6	1.950(5)	1.974

geometry with two *N*-methylimidazole ligands coordinated at both apical positions. This geometry is very similar to the one reported for the salen counterpart $[\mathbf{2\text{-}im}]^+$.[50] The two *N*-methylimidazole ligands are coordinated at the Co−N5 and Co−N6 bond distances 1.987(5) and 1.950(5) Å, respectively. The bond lengths in the equatorial plane Co−N1, Co−N2, Co−N3, and Co−N4 are 1.892(4), 1.898(4), 1.907(4), and 1.907(4) Å, respectively, with a very small angle between the N1−Co−N4 and N2−Co−N3 planes of 5.6°. As in $[\mathbf{2\text{-}im}]^+$ the equatorial coordination bonds are significantly elongated (ca. 0.05 Å) in $[\mathbf{1\text{-}im}]^+$ compared to **1**, pointing to a metal centered oxidation process (Co^{II}/Co^{III} redox couple). This is in excellent agreement with the analysis of the bond lengths of the two anilido groups which are essentially unaffected by oxidation.

The $[\mathbf{1\text{-}im}]^+$ complex was found to be paramagnetic in solution, as reflected by the broad ^1H resonances in $CDCl_3$. Since DFT calculations indicate that $[\mathbf{1\text{-}im}]^+$ in a singlet ground state is favored by 6 kcal/mol over the triplet state (high spin Co(III) metal ion or Co(II)-radical) and by 57 kcal/mol over the quintet ground spin state (high spin Co(II) metal ion coordinated to a radical), we propose that the paramagnetism stems from the release of one *N*-methylimidazole leading to a pentacoordinated complex. This proposal is in agreement with the electrochemistry experiments (see Electrochemistry section).

dx.doi.org/10.1021/ic402818g | *Inorg. Chem.* 2013, 52, 14428−14438

Table 6. Electrochemical Properties of 1, 2, and [1-im]$^+$

complex	$E_p^{a,0}$	$E_p^{c,0}$	$E_{1/2}^0$	$E_p^{a,1}$	$E_p^{c,1}$	$E_{1/2}^1$	$E_p^{a,2}$	$E_p^{c,2}$	$E_{1/2}^2$	$E_p^{a,3}$	$E_p^{c,3}$	$E_{1/2}^3$
1[a]		−2.44		−0.31	−0.37	**−0.34**	0.46	0.38	**0.42**	0.85	0.70	**0.78**
1[b]	−2.23	−2.29	**−2.26**	−0.31	−0.36	**−0.34**	0.40	0.34	**0.37**	0.60	0.53	**0.57**
2[a]				0.06	−0.04	**0.01**	0.65	0.75	**0.70**			0.74[c]
[**1-im**]$^{+a}$		−1.41		−0.45	−0.58	**−0.51**	0.07	−0.03	**0.03**	0.45		
[**1-im**]$^{+a,d}$				−0.60	−1.27	**−0.94**	0.06			0.38		

[a]In CH_2Cl_2 and 0.2 M TBA·BF_4. Potential values given in V vs the Fc^+/Fc reference electrode, T = 298 K. [b]In CH_3CN the presence of 0.2 M TBA·BF_4. Potential values given in V vs the Fc^+/Fc reference electrode, T = 298 K. [c]Measured by differential pulse voltammetry given the close proximity of $E_{1/2}$. [d]In the presence of 200 mol equiv of *N*-methylimidazole.

ELECTROCHEMISTRY

Redox Properties of 1. The square planar cobalt(II) complex **1** has been studied by cyclic voltammetry in the coordinating CH_3CN and noncoordinating CH_2Cl_2 solvents (+ 0.2 M $NBu4BF_4$). All potentials are referenced versus the Fc^+/Fc redox couple and summarized in Table 6. **1** is electro-active in the potential range −2.5 to +1.0 V. Let us first comment on the electrochemical behavior of **1** in CH_2Cl_2. The cyclic voltammogram (CV) of **1** displays three reversible one-electron redox waves in CH_2Cl_2 in the anodic region of potentials (Figure 8, Table 6). The redox process are observed at $E_{1/2}^1$ = −0.34 V, $E_{1/2}^2$ = 0.42 V, and $E_{1/2}^3$ = 0.78 V vs Fc^+/Fc. It is interesting to compare **1** with its salen counterpart **2**.[50] The CV of **2** also exhibits three reversible oxidation waves, at $E_{1/2}^1$ = 0.01 V, $E_{1/2}^2$ = 0.70 V, and $E_{1/2}^3$ = 0.74 V vs Fc^+/Fc in CH_2Cl_2, which were assigned to a metal-centered oxidation with a non-negligible contribution of the ligand to the SOMO for the former, followed by the successive formation of the Co^{3+}-phenoxyl and Co^{3+}-bis(phenoxyl) species according to eq 1.

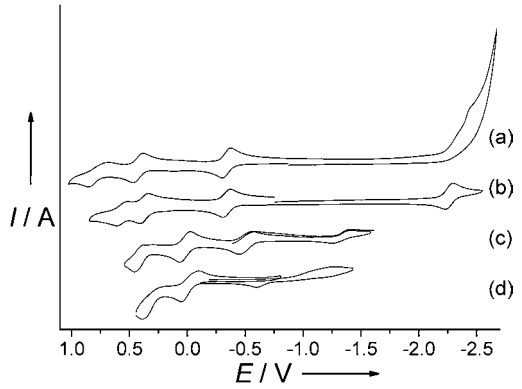

Figure 8. CV of 0.5 mM solutions of (a) **1** in CH_2Cl_2; (b) **1** in CH_3CN; (c) [**1-im**]$^+$ in CH_2Cl_2; (d) [**1-im**]$^+$ in CH_2Cl_2 + 200 equiv of *N*-methylimidazole; 0.2 M TBA.BF_4 was present in all solutions. The potentials are given vs Fc^+/Fc. Scan rate: 0.2 V/s; T = 298 K.

$$Co^{2+}\text{-L} \overset{E_{1/2}^1}{\rightleftharpoons} Co^{2+}\text{-L}^{\bullet} \text{ or } Co^{3+}\text{-L} \overset{E_{1/2}^2}{\rightleftharpoons} Co^{3+}\text{-L}^{\bullet} \overset{E_{1/2}^3}{\rightleftharpoons} Co^{3+}\text{-L}^{\bullet\bullet} \quad (1)$$

In **1** the potential values of the first and the second wave are strongly cathodically shifted as compared to **2**, while the third wave occurs at a similar potential, suggesting two ligand centered oxidations followed by the formation of the Co^{3+}-bis(anilinyl) species. This is supported by the fact that the potentials of the first and the second wave in **1** are similar to those of the corresponding nickel complex for which the oxidation has been shown to lead to the formation of the ligand mono- and diradical.[47] The CV of **1** measured in CH_3CN is presented in Figure 8b. The first and the second waves occur at similar potentials ($E_{1/2}^1$ = −0.34 and $E_{1/2}^2$ = 0.37 V, respectively) as in CH_2Cl_2, while the third one is found to be more reversible and shifted at lower potential ($E_{1/2}^3$ = 0.57 V). The trioxidized species is thus more accessible and stable in the presence of the coordinating CH_3CN solvent. Note that in this respect, Co^{3+}-salen complexes are known to be stabilized by coordination of exogenous ligands in axial positions, supporting the attribution of the third oxidation wave as a metal-centered oxidation process. The CV of **1** in CH_2Cl_2 additionally exhibits one irreversible reduction wave at $E_p^{c,0}$ = −2.44 V and a reversible wave at $E_{1/2}^0$ = −2.26 V in CH_3CN. Unfortunately, it turned out to be impossible to generate the reduced species either chemically or coulometrically, inhibiting characterization by spectroscopy and further investigation of the hydrogen production mechanism catalyzed by this complex described in the corresponding section. Nevertheless it is interesting to note that no reduction wave was present for the nickel complex, showing that the ligand is extremely robust toward reduction. This redox process is thus attributed to a metal-centered reduction process, formally concerning the Co^{II}/Co^{I} redox couple.

Redox Properties of [1-im]ClO_4. The CV of [**1-im**]$^+$ was measured in absence or in presence of excess *N*-methylimidazole in the medium and is shown in Figure 8. The CV of [**1-im**]$^+$ in the presence of 200 equiv of *N*-methylimidazole (Figure 8d) displays an irreversible reduction wave at $E_p^{c,1}$ = −1.27 V associated to an oxidation peak centered at $E_p^{a,1}$ = −0.60 V (peak separation ΔE_p^1 of 0.67 V), and two irreversible oxidation waves at $E_p^{a,2}$ = 0.06 V and $E_p^{a,3}$ = 0.38 V. A similar behavior has been reported for the salen counterpart [**2-im**]$^{+50}$ with 10 equiv of *N*-methylimidazole, where an irreversible reduction wave has been found at $E_p^{c,1}$ = −1.48 associated to an oxidation peak $E_p^{a,1}$ = −0.40 V (peak separation ΔE_p^1 of 1.08 V).[50] The reduction wave has been attributed to a metal-centered process, and the irreversibility of the wave is ascribed to the release of *N*-methylimidazole in the medium upon reduction, which yields the square planar cobalt(II) complex **2**.[50] The half wave potential for [**1-im**]$^+$ $E_{1/2}^1$ = −0.94 V, calculated as a midpoint potential between $E_p^{c,1}$ and $E_p^{a,1}$, is identical to that reported for [**2-im**]$^+$ in a medium containing CH_2Cl_2 + 10 equiv of *N*-methylimidazole.[50] This indicates that the redox process is metal-centered (Co(III)/Co(II) redox couple) in [**1-im**]$^+$ as was the case for [**2-im**]$^+$. However, the peak separation ΔE_p^1 is smaller in [**1-im**]$^+$ (0.67 V) than in [**2-im**]$^+$ (1.08 V). This could derive from a weaker coordination of the axial ligand upon reduction for [**1-im**]$^+$ as compared to [**2-im**]$^+$. Note that this is supported by the fact that addition of 200 equiv of *N*-methylimidazole is necessary to obtain this CV behavior as compared to only 10 equiv in the case of [**2-im**]$^+$ and that a much lower affinity for the axial ligand has been

dx.doi.org/10.1021/ic402818g | Inorg. Chem. 2013, 52, 14428−14438

reported for the nickel salen-anilido complexes compared to the salen counterpart.[50] Nevertheless, as for $[\mathbf{2\text{-}im}]^+$, the axial ligation by the *N*-methylimidazole base greatly stabilizes the cobalt(III) complex, as reflected by the lower $E_p^{a,1}$ of $[\mathbf{1\text{-}im}]^+$ when compared to **1**.

The CV of $[\mathbf{1\text{-}im}]^+$ measured in CH_2Cl_2 in the absence of additional *N*-methylimidazole is surprising (Figure 8c). $[\mathbf{1\text{-}im}]^+$ exhibits a reversible reduction wave at $E_{1/2}^{1} = -0.51$ V, followed by an irreversible reduction wave at $E_p^{c,0} = -1.41$ V. In the anodic scan two oxidation waves have been observed, the first one being reversible at $E_{1/2}^{2} = -0.03$ V and the second one irreversible at $E_p^{a,3} = 0.45$ V. The potential value $E_{1/2}^{1} = -0.51$ V is intermediate between that of $[\mathbf{1\text{-}im}]^+$ measured in presence of 200 equiv of *N*-methylimidazole ($E_{1/2}^{1} = -0.94$ V) and that of **1** ($E_{1/2}^{1} = -0.35$ V) measured in CH_2Cl_2. Thus, the CV of $[\mathbf{1\text{-}im}]^+$ in CH_2Cl_2 seems to reflect an intermediate case where the octahedral complex isolated as microcrystalline powder releases one of its axial *N*-methylimidazole ligands upon solvation in CH_2Cl_2, leading to a pentacoordinated species.

Electrochemical Properties of Complex 1 in the Presence of Acid and Bulk Electrolysis Experiments. The *p*-cyanoanilinium tetrafluoroborate acid ($pK_a = 7.0$ in acetonitrile) was found to be strong enough to protonate **1**.[55] Addition of 2 equiv of this acid results in the formation of $[\mathbf{H_21}](\mathbf{BF_4})_2$. The CV of **1** displays a reduction wave attributed to the $Co^{II/I}$ couple which is reversible in CH_3CN ($E_{1/2}^{0} = -2.26$ V), and irreversible in CH_2Cl_2 ($E_p^{c,0} = -2.44$ V). Interestingly, the CV of $[\mathbf{H_21}](\mathbf{BF_4})_2$ either in CH_3CN or in CH_2Cl_2 displays an irreversible wave for the reduction of Co^{II}, and the wave is shifted to positive potential by ~1 V compared to **1** (Supporting Information, Figure S11). Since both the pK_a and the standard redox potential are known for acetonitrile solutions of *p*-cyanoanilinium tetrafluoroborate, and not dichloromethane, the interpretation of the CVs recorded in acetonitrile with this acid is more meaningful.[55] In the presence of excess *p*-cyanoanilinium tetrafluoroborate, $[\mathbf{H_21}](\mathbf{BF_4})_2$ exhibits a catalytic wave (Figure 9). The background currents from the direct reduction of protons at the glassy carbon electrode are negligible at these potentials (Supporting Information, Figure S10), and the acid-induced current at these potentials can thus be attributed to catalytic turnover. The catalytic wave lies at a slightly more negative potential at high acid/catalyst concentration ratios than at lower ratios (Supporting Information, Figure S11). This could result from different catalytic mechanisms operative at low and high acid/catalyst ratios. An overpotential of 0.9 V has been calculated for $[\mathbf{H_21}](\mathbf{BF_4})_2$ using the Evans method (Supporting Information, Figure S10).[56]

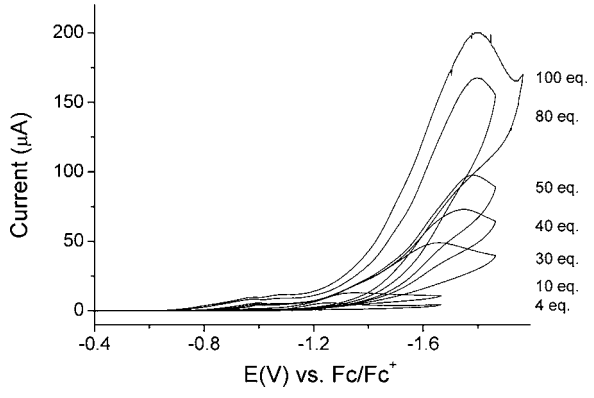

Figure 9. Successive cyclic voltammograms of a 0.5 mM solution of **1** in CH3CN at increasing concentrations of *p*-cyanoanilinium. Conditions: Scan rate = 200 mV s^{-1}, 0.2 M TBA·BF4 (supporting electrolyte), glassy carbon working electrode. Potentials are referenced vs Fc^+/Fc.

The CV features of electrocatalysis in Figure 9 uncover essential mechanistic details of the HER at cobalt macrocycles. This irreversible wave for the reduction of Co^{II} in Supporting Information, Figure S10 occurs in $[\mathbf{H_21}](\mathbf{BF_4})_2$ in absence of excess external acid near the position of the observed catalytic wave in the presence of acid. This indicates that the observed catalytic activity originates from the reaction of the reduced Co^{I} with the nearby proton belonging to the aniline groups.

To confirm that the above electrocatalytic process leads to hydrogen evolution, 3.7 h bulk electrolysis experiments of *p*-cyanoanilinium tetrafluoroborate salt in CH_3CN were carried out on a glassy carbon electrode at −1.9 V versus Fc/Fc^+ in the presence of catalytic amounts of **1**. Hydrogen evolution was monitored by GC analysis. From the amount of the electric charge flown through the electrode, an average turnover frequency of 8 h^{-1} and an average turnover number of 30 were calculated as described in the Supporting Information. No traces of other gas were detected by GC. Interestingly, a bulk electrolysis experiment of $[\mathbf{H_21}](\mathbf{BF_4})_2$ in MeCN or in CH_2Cl_2 at −1.50 V versus Fc/Fc^+ in absence of external acid source also allows us to detect hydrogen in small amounts, which confirms the hydrogen production from the protons carried by the bases in the first coordination sphere. The resulting reduced product has not been identified.

CONCLUSION

In summary, we have shown that an anilinosalen cobalt complex is capable of catalyzing the electrochemical reduction of protons. In this study, we show that the introduction of anilido groups instead of the classical phenolate groups in salen ligands allows the incorporation of proton relays in the first coordination sphere. To the best of our knowledge, **1** is the first cobalt based catalyst with a labile coordination sphere and with proton accepting donor group in the first coordination sphere. By a combination of spectroscopic, electrochemical, and theoretical studies, we show that the anilido groups in **1** can be protonated to give rise to $[\mathbf{H_21}](\mathbf{BF_4})_2$. $[\mathbf{H_21}](\mathbf{BF_4})_2$ exhibits interesting features: (1) acidic protons are carried by the anilino groups in the first coordination sphere, that is, adjacent to the reactive metal center (2) the complex is sufficiently flexible for the NH_2 groups to be able to adapt a staggered conformation. Further in-depth mechanistic studies, as well as attempts to lower the overpotential and to increase the pK_a of the bases in the first coordination sphere are ongoing work in our laboratories.

EXPERIMENTAL SECTION

Materials. Since **1** has been found to be slightly air sensitive, it was kept in a dry argon glovebox (MBraun LabMaster130), and all the corresponding samples for spectroscopic analysis are prepared in the glovebox. The solvents used for chemical reactions were purified by the solvent purification system MBraun MB SPS-800 Auto. The ligand $\mathbf{H_21}$ was synthesized according to published procedures.[47] The supporting electrolyte NBu_4BF_4 used for electrochemistry was purchased from Sigma-Aldrich and dried overnight at 100 °C under vacuum before use. Anhydrous acetonitrile or dichloromethane (>99.8%) used for electrochemistry and spectroscopic characterization were purchased from Sigma-Aldrich and stored in the glovebox.

dx.doi.org/10.1021/ic402818g | Inorg. Chem. 2013, 52, 14428−14438

Microanalysis were performed by the Service Central d'Analyze du CNRS (Lyon, France).

Spectroscopy. FTIR-spectra were recorded at room temperature on a Perkin-Elmer 2000 FT-IR spectrometer. Measurements in solid state were carried out in KBr pellets (3 mg sample in 300 mg KBr). NMR-spectra were recorded at room temperature using a Bruker DRX 400 spectrometer operating at 400.13 MHz for protons. Chemical shifts are given relative to tetramethylsilane (TMS) (listed in ppm). Absorption spectra were obtained using a diode-array UV−vis spectrometer (HP 8453). Absorption spectra of samples prepared in an anaerobic chamber were measured in 1 cm path length cuvettes sealed with a silicon stopper to retain anaerobic conditions, and spectra were measured quickly (<2 min.) after removing from the anaerobic chamber to avoid oxidation. No changes in the absorption spectra were observed over the time scale of these measurements. Continuous wave (CW) EPR measurements have been conducted on a Bruker Elexsys E500 spectrometer with an ER 4102ST-3731 resonator. Electron-spin−echo- (ESE-) detected EPR and ENDOR spectra were recorded on a Bruker Q-band Elexsys SuperQ FT EPR spectrometer equipped with a home-built EPR/ENDOR resonator[57] and an Oxford CF935 helium gas-flow cryostat. The EPR and ENDOR measurements were performed at 10 K. The microwave frequency was typically 33.9 GHz, with variations of 0.2 GHz, depending on the sample and the temperature. Pulsed ENDOR measurements were performed with a Davies ENDOR pulse sequence.[58] The accumulation time was typically several minutes for an EPR spectrum and 6−12 h for an ENDOR spectrum, depending on the sample and the magnetic field setting at which the ENDOR measurements were performed.

Electrochemistry. All electrochemical measurements were carried out under argon atmosphere at room temperature using an EG&G PAR 273A instrument. All solutions contained the supporting electrolyte NBu_4BF_4 (0.2 M in acetonitrile or dichloromethane). For cyclic voltammetry, a standard three-electrode configuration was used consisting of a glassy carbon (d = 2 mm) working and counter-electrodes and a Ag-wire placed in a $AgNO_3$ (0.01 M in MeCN)/NBu_4PF_6 (0.2 M in MeCN)-solution as a pseudoreference electrode. The system was systematically calibrated against ferrocene after each experiment, and all the potentials are therefore given versus the Fc/Fc^+ redox potential. *p*-Cyanoanilinium tetrafluoroborate was added by syringe as a 0.5 mol·L^{-1} solution in acetonitrile. After each addition of acid, the cyclic voltammogram was recorded immediately after a few seconds of stirring and once again after additional stirring for approximately 2 minutes. No significant changes were observed.

For the bulk electrolysis experiments, a glassy carbon stick electrode (d = 4.1 mm, l = 25 mm, A ~3.4 cm^2) was used, and the solutions were stirred during the electrolysis experiment to achieve better homogeneity. Electrolysis was performed at room temperature under argon atmosphere on solutions of the catalyst **1** (0.5 mmol L^{-1}) and *p*-cyanoanilinium acid (0.05 mol·L^{-1}) in acetonitrile (5 mL) at the constant potential of −1.8 V versus Fc/Fc^+ and on solutions of $[\mathbf{H_21}](\mathbf{BF_4})_2$ (2 mmol L^{-1}) in CH_2Cl_2 and (0.5 mmol L^{-1}) in CH_3CN at the constant potential of −1.5 V versus Fc/Fc^+. A blank experiment with a duration of 1000 s was performed to make sure that no significant amount of charge is consumed by the system without the catalyst (<4%). Note that this experiment was performed immediately after the bulk electrolysis experiment in the presence of the catalyst with the same working electrode only rinsed with CH_3CN showing that there is no deposit on the electrode surface that could be responsible for the electrocatalysis activity. Bulk electrolysis performed at room temperature under argon atmosphere on solution of the nonprotonated catalyst **1** (0.5 mmol L^{-1}) in acetonitrile (5 mL) at the constant potential of −2.5 V versus Fc/Fc^+ does not lead to hydrogen production. The evolving gas was identified as hydrogen throughout the whole electrolysis experiment using an Agilent 6890 gaschromatograph equipped with a 30 m Restek RT-Msieve 5 Å column and a thermal conductivity detector (TCD) thermostatted at 200 °C. Argon was used as a carrier gas, and the oven was thermostatted at 30 °C. Under these conditions, pure hydrogen has an evolution time of 110 s.

Crystal Structure Analysis. Single crystals of **1** and $[\mathbf{1\text{-}im}]\mathbf{ClO_4}$ were dipped into a mixture of polyparafins then taken up with a cryoloop and mounted on a Kappa CCD Nonius diffractometer equipped with graphite-monochromated Mo−Kα (λ = 0.71073 Å) and a cryostream cooler. Data collections were performed at 200 K. The cells were refined using the whole data respectively. Collected reflections were corrected for absorption,[59] Lorentz and polarization effects. The structures were solved by the charge flipping method implemented by OLEX2 software[60] and refined using the parallelized version of SHELX 97[61] run under OLEX2. All non- hydrogen atoms were refined with anisotropic thermal parameters. Hydrogen atoms were generated in idealized positions, attached to the carrier atoms, with isotropic thermal parameters.

A single crystal of $[\mathbf{H_21}](\mathbf{BF_4})_2$ was coated with perfluoropolyether, picked up with nylon loops and mounted in the nitrogen cold stream of the diffractometer. Mo−Kα radiation (λ = 0.71073 Å) from a Mo-target rotating-anode X-ray source equipped with INCOATEC Helios mirror optics was used. Final cell constants were obtained from least-squares fits of several thousand strong reflections. Intensity data were corrected for absorption using intensities of redundant reflections with the program SADABS.[59] The structures were readily solved by Patterson methods and subsequent difference Fourier techniques. The Siemens ShelXTL[62] software package was used for solution and artwork of the structures, ShelXL97[63] was used for the refinement. All non-hydrogen atoms were anisotropically refined, and hydrogen atoms were placed at calculated positions and refined as riding atoms with isotropic displacement parameters. The structure of $[H_21](BF_4)_2$ was found to be pseudocentric. Only carbon atoms of the cyclohexyl-backbone C(10) and C(12) do not fit inversion symmetry requirements (see checkcif alert in the Supporting Information) and show disorder when refined in space group $C2/c$. Finally, the structure was refined in space group $C2$ which appears to be the right choice since an enantiomerically pure cyclohexyldiamine was used for synthesis, disorder disappeared, and refinement parameters improved considerably. Crystallographic data of the compounds are listed in Table 1.

Computational Methods. All electronic structure calculations presented were carried out using the ORCA program package.[64] Full geometry optimizations were performed for all complexes using the GGA functional BP86[65,66] in combination with the Def2-TZV/P[67] basis set for all atoms and by taking advantage of the resolution of the identity (RI) approximation in the Split-RI-J variant[68] with the appropriate Coulomb fitting sets.[69] Increased integration grids (Grid4 in ORCA convention) and tight SCF convergence criteria were used. Solvent effects were accounted for according to the experimental conditions. For that purpose, we used the CH_2Cl_2 (ε = 38.3) solvent within the framework of the conductor like screening (COSMO) dielectric continuum approach.[70] The relative energies were obtained from single-point calculations using the B3LYP functional[65,66] together with the Def2-TZV/P[67] basis set. They were computed from the gas-phase optimized structures as a sum of electronic energy, thermal corrections to free energy, and free energy of solvation. Optical properties were also obtained from single-point calculations using the hybrid functional B3LYP[71,72] and the Def2-TZV/P[67] basis set. Electronic transition energies and dipole moments for all models were calculated using time-dependent DFT (TD-DFT)[73−75] within the Tamm-Dancoff approximation.[76,77] To increase computational efficiency, the RI approximation[78] was used in calculating the Coulomb term, and at least 30 excited states were calculated in the TD-DFT calculations.

Preparation of the Complexes. *1*. A methanolic solution of $Co(OAc)_2{\cdot}4H_2O$ (0.20 g, 0.92 mmol) and triethylamine (259 μL, 1.84 mmol) was added dropwise and under an inert atmosphere to a suspension of the $\mathbf{H_21}$ ligand (0.5 g, 0.92 mmol) in methanol. The resulting reaction mixture was stirred and heated at reflux for 1 h. The red precipitate appeared and was filtered, washed with cold methanol, and dried under vacuum. Single crystals of **1** were obtained by slow evaporation of a concentrated pyridinic solution. Yield: 0.42 g (76%). Anal. Calc. for $C_{36}H_{54}CoN_4$: C, 71.85; H, 9.04; N, 9.31; Co, 9.79.

Found: C, 70.08; H, 9.11; N, 9.32. ESI-MS m/z: 601.3 $[M]^+$. FTIR(KBr): 3314 cm^{-1} (s, NH).

[H21](BF4)2. Two equivalents of $HBF_4{\cdot}Et_2O$ were added to complex **1** (0.05 g, 0.083 mmol) in CH_2Cl_2 (4 mL) at room temperature in the glovebox, and the red solution turned immediately to yellow. The solution was stirred for a few minutes, and the solvent was removed completely. Quantitative synthesis. ESI-MS m/z: 301.6 $[M\text{-}2(BF_4)]^{2+}$. FTIR(KBr): 3314 (s, NH), 3376 (s, NH), 3232, (s, br, NH), 3139 (s, br, NH).

[1-im]ClO4. Three equivalents of 2-methylimidazole (0.499 mmol) were added to complex **1** (0.10 g, 0.166 mmol) in a methanol/CH_2Cl_2 solution (5/15 mL). The solution was stirred at room temperature under oxygenated atmosphere for 3 h and turned dark red. $NaClO_4{\cdot}H_2O$ (0.140 g, 0.998 mmol) in methanol (6 mL) was then added, and stirring at room temperature was continued for one day. Slow evaporation of the solvent gave dark red crystals after one day which were collected by filtration, washed with cold methanol, and dried under vacuum. Yield: 0.124 g (86%). Anal. Calcd for $C_{36}H_{54}CoN_4$:$C_{44}H_{66}ClCoN_8O_4$: C, 61.06; H, 7.69; N, 12.95; Co, 6.81. Found: C 60.04, H 7.32, N, 13.02. ESI-MS m/z: 715.4 $[M\text{-}2(im)\text{-}ClO_4]^+$.

■ ASSOCIATED CONTENT

Ⓢ Supporting Information

Details on spectroscopic, electrochemical, and computational investigation as well as crystallographic data. This material is available free of charge via the Internet at http://pubs.acs.org.

■ AUTHOR INFORMATION

Corresponding Authors

*E-mail: amelie.kochem@cec.mpg.de (A.K.).

*E-mail: maurice.van-gastel@cec.mpg.de (M.vG.).

Notes

The authors declare no competing financial interest.

■ ACKNOWLEDGMENTS

The authors thank G. Schmitz and M. Frenzer for their help with the GC experiments. This work was supported by the Max Planck Society.

■ REFERENCES

(1) Lewis, N. S.; Nocera, D. G. *Proc. Natl. Acad. Sci. U.S.A.* **2006**, *103*, 15729.

(2) Turner, J. A. *Science* **2004**, *305*, 972.

(3) Gray, H. B. *Nat. Chem.* **2009**, *1*, 7.

(4) Eisenberg, R.; Nocera, D. G. *Inorg. Chem.* **2005**, *44*, 6799.

(5) Frey, M. *ChemBioChem.* **2002**, *3*, 153.

(6) Fontecilla-Camps, J. C.; Volbeda, A.; Cavazza, C.; Nicolet, Y. *Chem. Rev.* **2007**, *107*, 4273.

(7) Darensbourg, M. Y.; Lyon, E. J.; Smee, J. J. *Coord. Chem. Rev.* **2000**, *206*, 533.

(8) Marr, A. C.; Spencer, D. J. E.; Schroder, M. *Coord. Chem. Rev.* **2001**, *219*, 1055.

(9) Darensbourg, M. Y.; Lyon, E. J.; Zhao, X.; Georgakaki, I. P. *Proc. Natl. Acad. Sci. U.S.A.* **2003**, *100*, 3683.

(10) Evans, D. J.; Pickett, C. J. *Chem. Soc. Rev.* **2003**, *32*, 268.

(11) Artero, V.; Fontecave, M. *Coord. Chem. Rev.* **2005**, *249*, 1518.

(12) Helm, M. L.; Stewart, M. P.; Bullock, R. M.; Rakowski DuBois, M.; DuBois, D. L. *Science* **2011**, *333*, 863.

(13) Wilson, A. D.; Shoemaker, R. K.; Miedaner, A.; Muckerman, J. T.; Dubois, D. L.; Rakowski DuBois, M. *Proc. Natl. Acad. Sci. U.S.A.* **2007**, *104*, 6951.

(14) Rakowski DuBois, M.; DuBois, D. L. *Chem. Soc. Rev.* **2009**, *38*, 62.

(15) Rakowski DuBois, M.; Dubois, D. L. *Acc. Chem. Res.* **2009**, *42*, 1974.

(16) Connolly, P.; Espenson, J. H. *Inorg. Chem.* **1986**, *25*, 2684.

(17) Hu, X. L.; Cossairt, B. M.; Brunschwig, B. S.; Lewis, N. S.; Peters, J. C. *Chem. Commun.* **2005**, *37*, 4723.

(18) Hu, X.; Brunschwig, B. S.; Peters, J. C. *J. Am. Chem. Soc.* **2007**, *129*, 8988.

(19) Dempsey, J. L.; Brunschwig, B. S.; Winkler, J. R.; Gray, H. B. *Acc. Chem. Res.* **2009**, *42*, 1995.

(20) Artero, V.; Chavarot-Kerlidou, M.; Fontecave, M. *Angew. Chem., Int. Ed.* **2011**, *50*, 7238.

(21) Du, P.; Eisenberg, R. *Energy Environ. Sci.* **2012**, *5*, 6012.

(22) Wang, M.; Chen, L.; Sun, L. *Energy Environ. Sci.* **2012**, *5*, 6763.

(23) Jacques, P. A.; Artero, V.; Pecaut, J.; Fontecave, M. *Proc. Natl. Acad. Sci. U.S.A.* **2009**, *106*, 20627.

(24) Stubbert, B. D.; Peters, J. C.; Gray, H. B. *J. Am. Chem. Soc.* **2011**, *133*, 18070.

(25) Jacobsen, G. M.; Yang, J. Y.; Twamley, B.; Wilson, A. D.; Bullock, R. M.; Rakowski DuBois, M.; DuBois, D. L. *Energy Environ. Sci.* **2008**, *1*, 167.

(26) Sun, Y.; Bigi, J. P.; Piro, N. A.; Tang, M. L.; Long, J. R.; Chang, C. J. *J. Am. Chem. Soc.* **2011**, *133*, 9212.

(27) Liu, T.; Darensbourg, M. Y. *J. Am. Chem. Soc.* **2007**, *129*, 7008.

(28) Gloaguen, F.; Rauchfuss, T. B. *Chem. Soc. Rev.* **2009**, *38*, 100.

(29) Kaur-Ghumaan, S.; Schwartz, L.; Lomoth, R.; Stein, M.; Ott, S. *Angew. Chem., Int. Ed.* **2010**, *49*, 8033.

(30) Appel, A. M.; DuBois, D. L.; Rakowski DuBois, M. *J. Am. Chem. Soc.* **2005**, *127*, 12717.

(31) Karunadasa, H. I.; Chang, C. J.; Long, J. R. *Nature* **2010**, *464*, 1329.

(32) Karunadasa, H. I.; Montalvo, E.; Sun, Y.; Majda, M.; Long, J. R.; Chang, C. J. *Science* **2012**, *335*, 698.

(33) Nicolet, Y.; de Lacey, A. L.; Vern_ede, X.; Fernandez, V. M.; Hatchikian, E. C.; Fontecilla-Camps, J. C. *J. Am. Chem. Soc.* **2001**, *123*, 1596.

(34) (a) Ott, S.; Kritikos, M.; Åkermark, B.; Sun, L.; Lomoth, R. *Angew. Chem., Int. Ed.* **2004**, *43*, 1006. (b) Schwartz, L.; Eilers, G.; Eriksson, L.; Gogoll, A.; Lomoth, R.; Ott, S. *Chem. Commun.* **2006**, 520. (c) Löscher, S.; Schwartz, L.; Stein, M.; Ott, S.; Haumann, M. *Inorg. Chem.* **2007**, *46*, 11094. (d) Jiang, S.; Liu, J.; Shi, Y.; Wang, Z.; Akermark, B.; Sun, L. *Dalton Trans.* **2007**, 896. (e) Barton, B. E.; Olsen, M. T.; Rauchfuss, T. B. *J. Am. Chem. Soc.* **2008**, *130*, 16834. (f) Wang, N.; Wang, M.; Liu, J.; Jin, K.; Chen, L.; Sun, L. *Inorg. Chem.* **2009**, *48*, 11551. (g) Lough, A. J.; Park, S.; Ramachandran, R.; Morris, R. H. *J. Am. Chem. Soc.* **1994**, *116*, 8356. (h) Park, S.; Lough, A. J.; Morris, R. H. *Inorg. Chem.* **1996**, *35*, 3001. (i) Xu, W.; Lough, A. J.; Morris, R. H. *Inorg. Chem.* **1996**, *35*, 1549. (j) Lee, D.-H.; Patel, B. P.; Clot, E.; Eisenstein, O.; Crabtree, R. H. *Chem. Commun.* **1999**, 297. (k) Crabtree, R. H.; Siegbahn, P. E. M.; Eisenstein, O.; Rheingold, A. L.; Koetzle, T. F. *Acc. Chem. Res.* **1996**, *29*, 348. (l) Chu, H. S.; Lau, C. P.; Wong, K. Y.; Wong, W. T. *Organometallics* **1998**, *17*, 2768. (m) Ayllon, J. A.; Sayers, S. F.; Sabo-Etienne, S.; Donnadieu, B.; Chaudret, B.; Clot, E. *Organometallics* **1999**, *18*, 3981. (n) Custelcean, R.; Jackson, J. E. *Chem. Rev.* **2001**, *101*, 1963. (o) Shook, R. L.; Borovik, A. S. *Inorg. Chem.* **2010**, *49*, 3646. (p) Yang, J. Y.; Nocera, D. G. *J. Am. Chem. Soc.* **2007**, *129*, 8192. (q) Yeh, C. Y.; C., J.; Nocera, D. G. *J. Am. Chem. Soc.* **2001**, *123*, 1513−1514.

(35) (a) Raugei, S.; Chen, S.; Ho, M. H.; Ginovska-Pangovska, B.; Rousseau, R. J.; Dupuis, M.; Dubois, D. L.; Bullock, R. M. *Chem.—Eur. J.* **2012**, *18*, 6493. (b) Rakowski DuBois, M.; DuBois, D. L. *Chem. Soc. Rev.* **2009**, *38*, 62. (c) Darensbourg, M. Y.; Lyon, E. J.; Smee, J. J. *Coord. Chem. Rev.* **2000**, *206*, 533.

(36) Wilson, A. D.; Shoemaker, R. K.; Miedaner, A.; Muckerman, J. T.; DuBois, D. L.; Rakowski DuBois, M. *Proc. Natl. Acad. Sci. U.S.A.* **2007**, *104*, 6951.

(37) Helm, M. L.; Stewart, M. P.; Bullock, R. M.; Rakowski DuBois, M.; Dubois, D. L. *Science* **2011**, *333*, 863.

(38) Barton, B. E.; Whaley, C. M.; Rauchfuss, T. B.; Gray, D. L. *J. Am. Chem. Soc.* **2009**, *131*, 6942.

(39) Barton, B. E.; Rauchfuss, T. B. *J. Am. Chem. Soc.* **2010**, *132*, 14877.

(40) Carroll, M. E.; Barton, B. E.; Gray, D. L.; Mack, A. E.; Rauchfuss, T. B. *Inorg. Chem.* **2011**, *50*, 9554.
(41) Schilter, D.; Nilges, M. J.; Chakrabarti, M.; Lindahl, P. A.; Rauchfuss, T. B.; Stein, M. *Inorg. Chem.* **2012**, *51*, 2338.
(42) Schilter, D.; Rauchfuss, T. B.; Stein, M. *Inorg. Chem.* **2012**, *51*, 8931.
(43) Manor, B. C.; Rauchfuss, T. B. *J. Am. Chem. Soc.* **2013**, *135*, 11895.
(44) (a) Kaur-Ghumaan, S.; Schwartz, L.; Lomoth, R.; Stein, M.; Ott, S. *Angew. Chem., Int. Ed.* **2010**, *49*, 8033. (b) Begum, A.; Sarkar, S. *Eur. J. Inorg. Chem.* **2012**, 40.
(45) Matsumoto, T.; Chang, H. C.; Wakizaka, M.; Ueno, S.; Kobayashi, A.; Nakayama, A.; Taketsugu, T.; Kato, M. *J. Am. Chem. Soc.* **2013**, *135*, 8646.
(46) (a) Bernhardt, P. V.; Jones, L. A. *Inorg. Chem.* **1999**, *38*, 5086. (b) Bond, A. M.; Lawrance, G. A.; Lay, P. A.; Sargeson, A. M. *Inorg. Chem.* **1983**, *22*, 2010.
(47) Kochem, A.; Gellon, G.; Leconte, N.; Baptiste, B.; Philouze, C.; Jarjayes, O.; Orio, M.; Thomas, F. *Chem.—Eur. J.* **2013**, DOI: 10.1002/chem.201303228.
(48) Chiang, L.; Kochem, A.; Jarjayes, O.; Dunn, J. T.; Vézin, H.; Sakaguchi, M.; Ogura, T.; Orio, M.; Shimazaki, Y.; Thomas, F.; Storr, T. *Chem.—Eur. J.* **2012**, *18*, 14117.
(49) Shimazaki, Y.; Arai, N.; Dunn, T. J.; Yajima, T.; Tani, F.; Ramogidab, C. F.; Storr, T. *Dalton Trans.* **2011**, *40*, 2469.
(50) Kochem, A.; Kanso, H.; Baptiste, B.; Aora, H.; Philouze, C.; Jarjayes, O.; Vezin, H.; Luneau, D.; Orio, M.; Thomas, F. *Inorg. Chem.* **2012**, *51*, 10557.
(51) (a) Klein, L. J.; Alleman, K. S.; Peters, D. G.; Karty, J. A.; Reilly, J. P. *J. Electroanal. Chem.* **2000**, *481*, 24. (b) Alleman, K. S.; Peters, D. G. *J. Electroanal. Chem.* **1998**, *451*, 121.
(52) Artero, V.; Chavarot-Kerlidou, M.; Fontecave, M. *Angew. Chem., Int. Ed.* **2011**, *50*, 7238.
(53) D., H. *Inorg. Chem.* **2006**, *45*, 9181. Penkert, F. N.; Weyhermüller, T.; Bill, E.; Hildebrandt, P.; Lecomte, S.; Wieghardt, K. *J. Am. Chem. Soc.* **2000**, *122*, 9663−9673.
(54) Karlsson., R.; Engelhardt., L. M.; Green., M. *J. Chem. Soc., Dalton Trans.* **1972**, 2463.
(55) Fourmond., V.; Jacques., P. A.; Fontecave., M.; Artero., V. *Inorg. Chem.* **2010**, *49*, 10338.
(56) Felton, G. A. N.; Glass, R. S.; Lichtenberger, D. L.; Evans, H. *Inorg. Chem.* **2006**, *45*, 9181.
(57) Lendzian, F.; Bittl, R.; Lubitz, W. *Photosynth. Res.* **1998**, *55*, 189.
(58) Schweiger, A.; Jeschke, G. *Principles of Pulse Electron Paramagnetic Resonance*; Oxford University Press: Oxford, U.K., 2001.
(59) Sheldrick, G.M. *SADABS, Bruker−Siemens Area Detector Absorption and Other Correction*, Version 2008/1; University of Göttingen: Göttingen, Germany, 2006.
(60) Dolomanov, O. V.; Bourhis, L. J.; Gildea, R. J.; Howard, J. A. K.; Puschmann, H. *J. Appl. Crystallogr.* **2009**, *42*, 339.
(61) Sheldrick, G. M. *Acta Crystallogr.* **2008**, *A64*, 112.
(62) *ShelXTL* 6.14; Bruker AXS Inc.: Madison, WI, 2003.
(63) Sheldrick, G. M. *ShelXL97*; University of Göttingen: Göttingen, Germany, 1997.
(64) Neese, F. *WIREs Comput. Mol. Sci.* **2012**, *2*, 73.
(65) (a) Perdew, J. P. *Phys. Rev. B* **1986**, *33*, 8822. (b) Perdew, J. P. *Phys. Rev. B* **1986**, *34*, 7406.
(66) Becke, A. D. *Phys. Rev. A* **1988**, *38*, 3098.
(67) Weigend, F.; Ahlrichs, R. *Phys. Chem. Chem. Phys.* **2005**, *7*, 3297.
(68) Neese, F. *J. Comput. Chem.* **2003**, *24*, 1740.
(69) Weigend, A. *Phys. Chem. Chem. Phys.* **2006**, *8*, 1057.
(70) Klamt, A.; Schürmann, G. *J. Chem. Soc., Perkin Trans. 2* **1993**, 793.
(71) Becke, A. D. *J. Chem. Phys.* **1993**, *98*, 5648.
(72) Lee, C.; Yang, W.; Parr, R. G. *Phys. Rev. B* **1988**, *37*, 785.
(73) Casida, M. E. In *Recent Advances in Density Functional Methods*; Chong, D. P., Ed.; World Scientific: Singapore, 1995.
(74) Stratmann, R. E.; Scuseria, G. E.; Frisch, M. J. *J. Chem. Phys.* **1998**, *109*, 8218.
(75) Bauernschmitt, R.; Ahlrichs, R. *Chem. Phys. Lett.* **1996**, 454.
(76) Hirata, S.; Head-Gordon, M. *Chem. Phys. Lett.* **1999**, *314*, 291.
(77) Hirata, S.; Head-Gordon, M. *Chem. Phys. Lett.* **1999**, *302*, 375.
(78) Neese, F.; Olbrich, G. *Chem. Phys. Lett.* **2002**, *362*, 170.